J. Fluid Mech. (2024), *vol*. 996, A48, doi:10.1017/jfm.2024.837

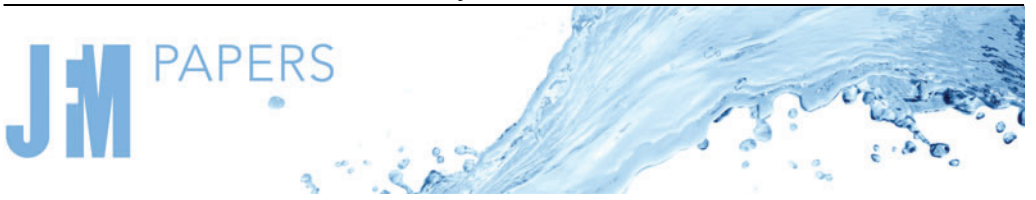

Yield stress fluids solidifying in capillary imbibition

Hanul Kim[1] **and Siyoung Q. Choi**[1,2,†]

[1]Department of Chemical and Biomolecular Engineering, Korea Advanced Institute of Science and Technology (KAIST), 291 Daehak-ro, Yuseong-gu, Daejeon 34141, Republic of Korea

[2]KAIST Institute for the Nanocentury, Korea Advanced Institute of Science and Technology, 291 Daehak-ro, Yusseong-gu, Daejeon 34141, Republic of Korea

(Received 27 December 2023; revised 28 July 2024; accepted 27 August 2024)

When subjected to external stress exceeding their yield stress (σ_Y), yield stress fluids (YSFs) undergo transition from solid to liquid. While the flow dynamics of capillary flows – including wetting, coating, spreading, and wicking – can be predicted accurately for fluids without yield stress, only a few asymptotic solutions have been validated against experiments for YSFs. In this study, we explore experimentally and theoretically the entire dynamics and solidifying process during capillary imbibition of YSFs, representing the fundamental aspect of capillarity-driven flow. We observe that during the gradual deceleration of capillary rise, YSFs exhibit apparent flow below σ_Y. This unexpected behaviour is linked to wall slip, manifested as plug flow in particle image velocimetry analyses. We introduce a model with numerical solutions, grounded in the rheological properties of YSFs and slip mechanisms, to accurately describe this liquid–solid transitional behaviour.

Key words: capillary flows, wetting and wicking

1. Introduction

A yield stress fluid (YSF) keeps its shape like a solid until a sufficiently large stress ($> \sigma_Y$) initiates a liquid-like flow (Coussot *et al.* 2002; Bonn *et al.* 2017). Such YSFs are widely found in biofluids (cell medium and mucus) (Hu *et al.* 2015), as well as in various industries, such as paintings, cosmetics and foods. For YSFs, the solid-to-liquid change is the key flow behaviour commonly denoted as yielding (Møller, Fall & Bonn 2009; Balmforth, Frigaard & Ovarlez 2014; Malkin, Kulichikhin & Ilyin 2017; Coussot 2018; McConnell *et al.* 2022; Dey *et al.* 2023) or fluidization (Bocquet, Colin & Ajdari 2009; Benzi *et al.* 2019, 2021; Garg *et al.* 2021; Jadhav, Rossi & Karimfazli 2021).

† Email address for correspondence: sqchoi@kaist.ac.kr

The yielding depends on the strain rate and stress, and shows a gradual transition rather than a sudden event (Oldroyd 1947; Bonn & Denn 2009; Coussot & Rogers 2021). Since plastic deformation takes place after elastic response, stress overshoot appears as a consequence of microstructural rearrangement, and transient/permanent shear banding follows due to its inhomogeneity (Benzi *et al.* 2021).

Contrary to yielding, which is a transition from solid to liquid under stress exceeding σ_Y, solidification in YSFs represents a liquid-to-solid transition as stress decreases below σ_Y. The disparity between dynamic and static yield stresses suggests that the solidification process differs fundamentally, requiring a distinct analytical approach (Divoux, Barentin & Manneville 2011; Chaudhuri, Berthier & Bocquet 2012; Balmforth *et al.* 2014). Solidification processes have been studied across diverse contexts, ranging from time-dependent simple shear scenarios to the cessation of motion in particles, bubbles, and droplets (Huilgol, Mena & Piau 2002; Matson & Hogg 2007; Tokpavi, Magnin & Jay 2008; Tsamopoulos *et al.* 2008; Sikorski, Tabuteau & de Bruyn 2009; Dimakopoulos, Pavlidis & Tsamopoulos 2013; Damianou *et al.* 2014; Jalaal *et al.* 2018; Huilgol, Alexandrou & Georgiou 2019). It has been shown that the criteria for cessation are influenced by factors including yield stress, stress during solidification, surface tension, and relaxation time. Given its prevalence in capillarity-driven flows like wetting, coating, spreading and wicking (Huilgol & Kefayati 2018), solidification warrants specific attention within the scope of capillary imbibition. While a few models address the flow dynamics of YSFs during solidification (Bertola 2009; Géraud *et al.* 2014; Huilgol & Kefayati 2018; Balmforth 2019) and compare them with experimental results (Balmforth, Ghadge & Myers 2007; Jalaal, Stoeber & Balmforth 2021; van der Kolk, Tieman & Jalaal 2023), mostly they focus on the asymptotic solution for the final state ($t \to \infty$). Notably, none has been compared directly with the experimental dynamics throughout the entire wetting process.

In this work, our primary focus is the solidification of YSFs in capillary rise (figure 1*a*). From the conservation of momentums acting on the liquid (density ρ), the wall shear stress on a capillary inner surface with a sufficiently narrow radius R is a function of rise height ($h(t)$) as expressed by

$$\sigma_w(t) = \frac{\Gamma \cos\theta_E}{h(t)} - \frac{\rho g R}{2}, \tag{1.1}$$

with the constitutive equation for Newtonian and shear thinning fluids,

$$\dot{h}(t) = \frac{R}{s+2}\left(\frac{\sigma_w(t)}{K}\right)^{s-1}, \tag{1.2}$$

where Γ is the surface tension of the liquid–air interface, θ_E is the equilibrium contact angle between the liquid and the capillary, g is the gravitational constant, K is the consistency parameter, n is the thinning power, and $s = 1/n + 1$ (Lucas 1918; Washburn 1921; Rideal 1922). Equation (1.2) can be generalized for the Newtonian fluid by putting $n = 1$ and K as the viscosity. Because $h(t)$ increases in time, $\sigma_w(t)$ finally converges to zero for typical constitutive equations (Newtonian or shear thinning fluid). This corresponds to a monotonic rise curve of aqueous glycerol in figure 1(*b*). The YSFs, however, undergo solidification at $h_p = \Gamma \cos\theta_E/(\sigma_Y + \rho g R/2)$, the height where $\sigma_w = \sigma_Y$ (Balmforth 2022). We found that the solidification slows down YSFs at h_p, but is followed by another onset of capillary rise, as in figure 1(*c*). This contradicts a previous study that says a YSF stops at h_p (Géraud *et al.* 2014). Instead, slip attributes the flow after the solidification. Our proposed model predicts the complete capillary rise of YSFs quite accurately, and explains

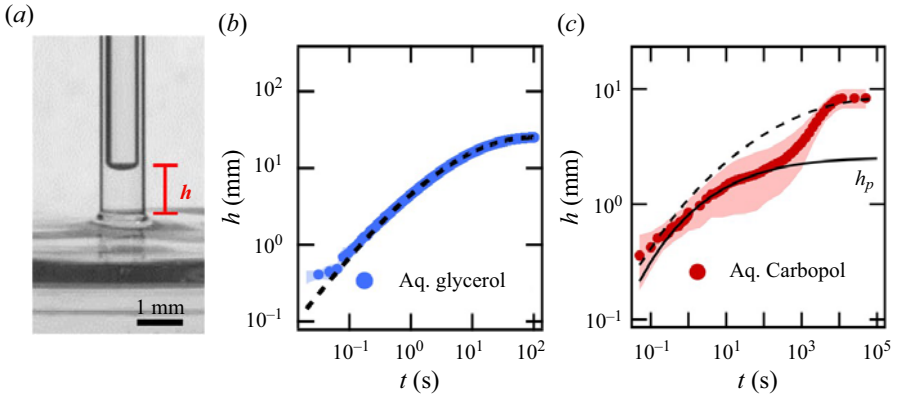

Figure 1. (*a*) Schematic for the capillary rise experiment. Capillary rise $h(t)$ of (*b*) 85 % glycerol (Newtonian fluid, $\sigma_Y = 0$) and (*c*) 0.12 wt. % Carbopol (YSF, $\sigma_Y = 10$ Pa). Dashed lines in (*b*,*c*) are (1.1) combined with (1.2) for Newtonian and simple power law fluids ($\sigma_Y = 0$), respectively. The solid line is (1.1) with (2.1). The shading is an error bar. Experimental parameters follow table 1.

what determines the flow dynamics after solidification based on the relevant length and time scales.

2. Results and discussion

Figure 1(*b*) shows that Newtonian fluids show a monotonic increase until reaching equilibrium height ($h_E = 2\Gamma \cos\theta_E/\rho g R$), where Laplace pressure is balanced by gravity (see Appendix A for experimental details). The model curve aligns with Newtonian fluid data when Hagen–Poiseuille flow is assumed. However, in figure 1(*c*), the model fails to match for YSFs with a simple power-law fluid, possibly due to the presence of yield stress and inability to account for yielding or solidification impacts.

Accordingly, a well-known Herschel–Bulkley (HB) model is implemented to replace (1.2). For $\sigma > \sigma_Y$, $\sigma = \sigma_Y + K\dot{\gamma}^n$, where $\dot{\gamma}$ is the shear rate. When $\sigma \le \sigma_Y$, $\dot{\gamma} = 0$. The apparent rise velocity $\dot{h}(t)$ is obtained by averaging the shear rate in radial direction: $\dot{h}(t) = \int_0^R 2\pi r\,\dot{\gamma}(r,t)\,\mathrm{d}r$ (Sochi & Blunt 2008; Pérez-González *et al.* 2012). By replacing the shear rate with the HB model, it rearranges and explicitly links $\dot{h}(t)$ to the wall shear stress ($\sigma_w(t)$) as

$$\dot{h}_{HB}(t) = R\left(\frac{\sigma_w(t)}{K}\right)^{s-1} f(\epsilon(t), s), \tag{2.1}$$

where

$$f = (1-\epsilon(t))^s \left\{\frac{(1-\epsilon(t))^2}{s+2} + \frac{2\epsilon(t)\,(1-\epsilon(t))}{s+1} + \frac{\epsilon(t)^2}{s}\right\}, \quad \epsilon(t) = \frac{\sigma_Y}{\sigma_w(t)} < 1. \tag{2.2}$$

For regime $\epsilon(t) \ge 1$, $\dot{h} = 0$. Upon applying $\epsilon = 0$, (2.1) reduces to (1.2), where f becomes $1/(2+s)$.

With the implementation of (2.1), the numerical solution with measured σ_Y is shown as a solid line in figure 1(*c*) (see Appendix B for the rheology measurement result). The plateau height, denoted as h_p, was determined precisely by the model. This indicates that the plateau is a result of the solidification process of the YSF. For all the theoretical curves, dynamic contact angle (DCA) theory is employed to account for the wetting friction of

YSF	Conc. (wt. %)	σ_{HB} (Pa)	σ_Y (Pa)	n	Γ (mN/m)	R (mm)	K (Pa s^n)	l_s (nm)
Carbopol	0.12	10	10	0.4	38	0.85	11	0.4
	0.08	3.5	1.5	0.4	60	0.85	3.5	15
Xanthan	1.3	10	44	0.4	36	0.42	1.9	13
	1.0	7.8	19	0.5	53	0.42	0.7	14
	0.7	4.5	4.5	0.4	58	0.42	0.8	20
	0.3	<0.05	0.9	0.2	63	0.42	0.8	55

Table 1. Rheological properties and slip layer thicknesses: σ_{HB} is fitted from a rheology measure, while σ_Y is fitted from capillary rise $h(t)$. Theoretical prediction follows σ_Y.

the meniscus (Kim *et al.* 2020). The DCA description and its fitting are available in Appendix C and figures 5(*a*,*b*) below. The YSF surface tension is estimated from the Laplace pressure at $h_E = h(t \to \infty)$ due to the lack of reproducibility of the previously proposed method, which heavily relies on the selection of geometry (Jørgensen *et al.* 2015; Jalaal *et al.* 2021). The measured surface tension is given in table 1, where its value varies by polymer concentration. These values can be considered as apparent surface tensions acting on a capillary imbibition system, since the value can be hindered dynamically by the yield stress (Martouzet *et al.* 2021).

Interestingly, stress overshoot has negligible impact on the macroscale dynamics of capillary rise. Recent experimental and theoretical studies have demonstrated that the transition from solid to liquid is accompanied by a stress overshoot, as evidence of plastic deformation of YSF (Donley *et al.* 2020; Kamani, Donley & Rogers 2021). In a case of the capillary rise, the good fit of (2.1) to the initial rising speed indicates that stress overshoot has little effect on the macroscale flow dynamics; with a sufficiently large Laplace stress ($\sigma \sim 100$ Pa) at the beginning, the characteristic time scale for yielding rate ($\sim 10^{-2}$ s) is an order of magnitude faster than the time scale of our measurements ($\geq 10^{-1}$ s) (Benzi *et al.* 2021).

As shown in figure 1(*c*), the experimental curve of YSFs shows a significant deviation from the saturation predicted by (2.1) (solid line) and continues to rise until h_E. Derived from (1.1), which is relevant to all instances of capillary rise irrespective of the fluid's rheological characteristics, it is observed that the wall shear stress diminishes with an increase in penetration length. Hence the rise beyond h_p is indicative of a decline in wall shear stress. Ultimately, this anomalous flow behaviour is associated with the culmination of the liquid-to-solid transition, during which shear stress continues to decrease even after surpassing σ_Y. This makes solidification distinct from the re-entrance effect under long-term creep tests (Landrum, Russel & Zia 2016) and thixotropic aging (Choi, Armstrong & Rogers 2021). One possibility is that YSFs may not undergo complete solidification, as seen in the analogy of delayed yielding (Landrum *et al.* 2016). This approach emphasizes the rheological inhomogeneity of YSF and incorporates local mobility as a function of shear stress and shear rate (Benzi *et al.* 2021). Another possibility is that a YSF flows after h_P as a 'gliding solid block'. The experiments can be explained by the presence of a shallow lubrication layer near the wall, where high shear stress is concentrated. The slip of YSFs is common, regardless of their yielding mechanism, chemical composition, geometry or wall surface roughness (Piau 2007; Damianou *et al.* 2014; Zhang *et al.* 2017; Jalaal *et al.* 2018).

In order to verify the aforementioned hypotheses, the flow velocity is visualized with the particle image velocimetry (PIV) method. We expect a plug flow in the case of an

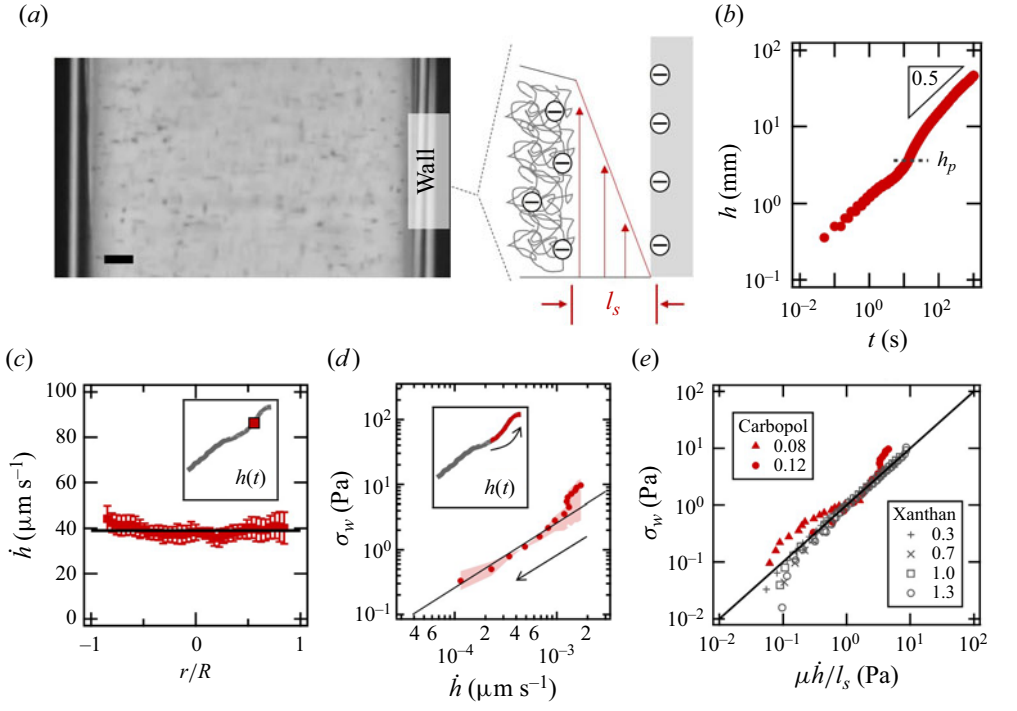

Figure 2. (*a–c*) Slip demonstration of horizontal imbibition using 0.12 wt. % Carbopol. (*a*) Microscope image of 0.12 wt. % Carbopol inside a glass capillary. The solution is seeded with 10 μm hollow glass spheres. The scale bar is 100 μm. The scheme on the right describes the depletion layer at the YSF–glass interface. (*b*) Horizontal capillary imbibition curve. (*c*) The PIV analysis result. The solid line is the plug flow velocity profile from the bulk imbibition speed. (*d,e*) Stress-velocity plots during the vertical capillary imbibition for (*d*) 0.12 wt. % and (*e*) various YSFs. The solid line is the Newtonian slip model (2.4). The shading in (*d*) shows the error bar. Insets in (*c,d*) show the vertical capillary rise curve $h(t)$, and coloured markers denote corresponding regimes. Velocity in (*e*) is normalized with μ and l_s. The concentrations in the legend in (*e*) are given in wt. %.

entire solid, otherwise a curved velocity profile for a mixed solid–fluid state. An example optical image is shown in figure 2(*a*). Experimental details for PIV measurement are given in Appendix D. The velocity profile was analysed during horizontal imbibition due to its convenience of imaging. This method remains valid as a YSF solidifies even in the absence of gravity, and the penetration curve exhibits a plateau similar to that of the vertical rise (figure 2*b*). The velocity profile depicted in figure 2(*c*) is indeed a plug, suggesting that the fluid undergoes complete solidification instead of existing in a state of mixture between solid and liquid.

To confirm the slip effect, the wall shear stresses are examined from all the points after the plateau. Because the wall shear stress can be computed simply by the rise (h) using (1.1), it is independent of the constitutive relationship to the fluid viscosity. In figure 2(*d*), when the height of the vertical capillary rise is converted into the wall shear stress, it shows the wall shear stress increases linearly with the rise velocity. Even if the experimental stress at the regime with high velocity shows a higher value than the theoretical prediction, it lies in the theoretical model when the lower bound of the error bar is accounted for. Moreover, the same relation has been found even more clearly in other vertical capillary rises of xanthan solutions (grey markers in figure 2*e*), as well as other YSFs shown in Zhang *et al.*

(2017). In other words, even if the apparent viscosity changes, YSFs share similar slip behaviour at boundaries.

To implement slip, a Newtonian slip model (Zhang *et al.* 2017) is added to (2.1). The slip layer has thickness l_s, in which polymers are depleted. When its viscosity is assumed as the solvent viscosity (μ), the slip velocity can be written with wall shear stress proportionally as

$$\dot{h}_{slip}(t) = \frac{l_s \sigma_Y}{\mu\, \epsilon(t)}, \tag{2.3}$$

which is added to $\dot{h}_{HB}(t)$ as

$$\dot{h}(t) = \dot{h}_{slip}(t) + \dot{h}_{HB}(t). \tag{2.4}$$

Even though other slip models have been suggested in Damianou *et al.* (2014), it has been demonstrated that these various models converge to a linear model when the edge evaporation effect is removed (Zhang *et al.* 2017). Therefore, in our evaporation-controlled study, we consider the linear model, which still shows great accordance with experimental data within the error range.

Equation (2.4) is connected with (1.1), and the value of l_s is determined by fitting the slope in the stress–velocity plot, the linear plot of figure 2(*d*). The slip gradually develops even before solidification when $h < h_p$, but the slip's effect on the rising speed is negligible as $\sigma_Y \ll \sigma_w(t)$. After the solidification, the slip itself takes on the role of the apparent speed as the YSF is not flowing, considering that the contribution from (2.1) is zero with $\sigma_w(t) < \sigma_Y$. Due to the discontinuity of (2.1) between regimes before and after h_p, the numerical calculation explicitly connects the two regimes. The final solution of the early regime, which includes h, $\dot{h}$ and σ_w, serves as the initial condition after h_p.

In figures 3(*a*,*b*), the solid lines represent the capillary rise prediction of (1.1) and (2.4) for different YSFs. The experimental data are plotted using colour markers to indicate the yield stress. The rheological properties, surface tension and l_s are given in tables 1 and 2. Surprisingly, model curves are capable of effectively capturing the diverse dynamics of capillary rise. The transition from solidification to gliding flow is accurately described smoothly, as supported by experimental results.

To better reflect the initial trajectory of 1.3 and 1.0 wt. % xanthan solutions, the yield stress was fitted empirically from the rise curve. This is due to the ambiguity in the yield stress determination for xanthan (Barnes & Walters 1985; Tang *et al.* 2018). The residual discrepancy can be explained with shear banding, as shown in Appendix E. By reducing the shear banding effect with salt (Tang *et al.* 2018), experimental data follow the proposed model very well. To be within the scope of this work, accurate prediction of shear banding (de Souza Mendes 2011) is not included here. Although the Carbopol 0.08 wt. % sample's yield stress is also fitted, a plateau curve appears and could be interpreted with our proposed model, when the surface is altered into a less slippery condition through surface silanization (see Appendix E and figure 6*b*). The lowest concentration for which Carbopol maintains yield stress characteristics is 0.08 wt. %, as highlighted by Jaworski *et al.* (2022), suggesting potential shear thinning behaviour under rapid flow conditions. Under conditions of a slippery surface, initial penetration speed is notably quicker compared to scenarios involving a silanized surface, where the pace significantly diminishes. The yield stress values σ_Y, deduced from the $h(t)$ profiles, are used for the theoretical prediction in figures 3(*a*) and 3(*b*), with values listed in table 1. Concurrently, the table also presents σ_{HB} values, derived from rheological analyses detailed in Appendix B.

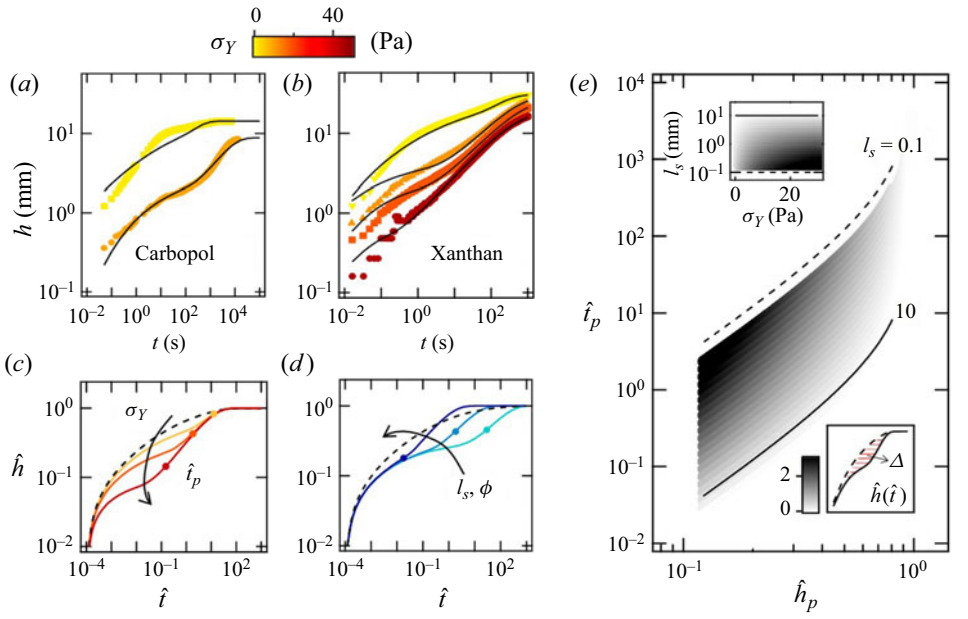

Figure 3. (*a*,*b*) Proposed model prediction (solid lines) against experiments. From top to bottom, concentrations are 0.08 and 0.12 wt. % in (*a*), and 0.3, 0.7, 1.0 and 1.3 wt. % in (*b*). Marker colours match the colour map for σ_Y. (*c*,*d*) Normalized numerical solutions of (1.1) and (2.4) varying yield stress and slip conditions. From the bottom, (*c*) $\sigma_Y = 40$, 10 and 2 Pa, while (*d*) $(l_s, \phi) = (0.01\ \text{nm}, 0.006)$, $(0.2\ \text{nm}, 0.1)$ and $(16\ \text{nm}, 9)$ nm. Dashed lines in (*c*,*d*) are shear thinning curves without slip. (*e*) Contour plot of Δ. The solid line shows $l_s = 10$ nm, and the dashed line is $l_s = 0.1$ nm. The lower inset is the graphical definition of Δ, while the upper inset shows the same contour over l_s versus σ_Y. For (*c*–*e*), rheological properties other than σ_Y, surface tension and DCA parameters follow the Carbopol 0.12 wt. % values shown in table 1 and table 2.

The plateau shows diverse intensities and shapes in both our experiments and the theoretical model. It can be expected that a larger yield stress results in a stronger plateau. In figure 3(*b*), the plateau at 1.3 wt. % xanthan solution in the darkest colour marker, however, is less pronounced and nearly unnoticeable as compared to the lower concentrations. It can be inferred that the strength of a plateau might be determined not solely by the yield stress, but also by other variables such as slip and consistency parameter (K).

Based on the proposed model, the various intensities and shapes of the plateau are studied theoretically. Capillary rise curves were obtained in figures 3(*c*) and 3(*d*) by changing only the rheology or slip, respectively, in order to distinguish the effects from each factor. All axes are normalized, where $\hat{h}$ is the rise height divided by the final height (h_E), and $\hat{t}$ is the time divided by the characteristic time scale of capillary rise (t_v, which is defined without yield stress and given in table 2) (Kim *et al.* 2020).

In figure 3(*c*), an increase in the yield stress slows down the rise speed, and the plateau appears earlier. Figure 3(*d*) depicts the variation of slip strength while assuming a constant yield stress. In order to assess the contribution of slip at the plateau, the velocity ratio (ϕ) is obtained by dividing the slip contribution ($\dot{h}_{slip}$) by the non-slip contribution ($\dot{h}_{HB} = \dot{h} - \dot{h}_{slip}$). At the point where the slip and non-slip velocities experience the same stress around the plateau, ($\sigma_w = 2\sigma_Y$), we have

$$\phi = \frac{\dot{h}_{slip,\epsilon=0.5}}{\dot{h}_{HB,\epsilon=0.5}} = \frac{8\, g(n)\, l_s}{R\mu}\left(\frac{K}{{\sigma_Y}^{1-n}}\right)^{1/n}, \tag{2.5}$$

YSF	Conc. (wt. %)	χ_1	χ_2	θ_E (deg.)	t_p (s)	t_v (s)	h_p (mm)	ϕ	Δ
Carbopol	0.12	2.3	0.04	14.5	664	867	2.6	0.1	2.1
	0.08	1.0	0.60	<5	92	60	6.6	0.9	0.4
Xanthan	1.3	6.1	0.21	<5	1	171	2.9	0.01	3.4
	1.0	15	0.44		10	33	5.4	0.01	4.2
	0.7	12	0.42		18	35	8.8	0.01	3.7
	0.3	55	3.50		424	27	30	1.6	0.6

Table 2. DCA model parameters, slip dominance and plateau intensity.

where $g(n) = (n+1)(2n+1)(3n+1)/n(7n^2+8n+2)$. The two graphs (figures 3*c*,*d*) are completely different, suggesting that each has a unique impact on the capillary rise dynamics. The position of the plateau and the transitional rate of rise are determined mainly by the yield stress, whereas the persistence of solidification and the rate of later rise are affected by slip.

The time scale for the duration of the plateau (t_p) is derived via dividing plateau height by slip velocity, as

$$t_p = \frac{h_p}{\dot{h}_{slip,\epsilon=1}} = \frac{h_E \mu}{l_s \sigma_Y \left(1 + \dfrac{2\sigma_Y}{\rho g R}\right)}. \tag{2.6}$$

We define $\hat{t}_p$ as t_p divided by t_v, shown by dots on the solid lines in figures 3(*c*) and 3(*d*). Solidification finishes faster for higher yield stress and more slippery cases. It is interesting to note that when l_s is reduced below a single atomic size, t_p extends beyond 10^3 s. According to Zhang *et al.* (2017), this duration is sufficient for the evaporation-induced residual stress to build up at the edge. The evaporation at the edge slows down the capillary imbibition speed because it affects primarily the wetting friction of the meniscus (Zhao *et al.* 2019). In Young's spreading of YSFs on rough surfaces, a similar cessation occurs when the plateau phase persists long enough for the meniscus edge to fully dry out (Géraud *et al.* 2014). Our observation of additional flow and its interpretation by incorporating the slip model distinguish our findings from the previous models and experiments (Balmforth 2022), where lubrication theory is applied identically in Hele-Shaw cell geometry. On the other hand, the previous no-slip asymptotic rise curve can be derived from the present model by assuming an extremely short l_s and minimizing the DCA effect.

For a general understanding of the plateau intensity, we evaluated the flexion of plateau (Δ) as

$$\Delta = \int_0^\infty (\tilde{h}_0(\tilde{t}) - \tilde{h}(\tilde{t}))\, \mathrm{d}\tilde{t}, \tag{2.7}$$

where $\tilde{t}$ and $\tilde{h}$ are logarithmic $\hat{t}$ and $\hat{h}$, and $\tilde{h}_0$ is the normalized logarithmic rise height with $\sigma_Y = 0$. As shown in the bottom inset $h(t)$ curve of figure 3(*e*), Δ is the integration of the difference in height between curves $\tilde{h}_0$ and $\tilde{h}$. The intensity is calculated by varying σ_Y and l_s as shown on the plane of the normalized plateau time and height. According to the presented phase diagram, it can be observed that the plateau strength is positively correlated with the magnitude of the yield stress, while exhibiting an inverse relationship with the degree of slip. Even if the solidification occurs early (low $\hat{h}_p$), the flow can closely resemble the dynamics of shear thinning fluids when they experience a large slip effect

(low $\hat{t}_p$), as well as in high $\hat{h}_p$ cases. The enhancement of slip can be obtained in cases of the increasing thickness of the slip layer (e.g. the enhancing repulsive forces between the YSF element and the smooth wall).

3. Conclusions

This study revisits the capillary imbibition problem in yield stress fluids (YSFs), demonstrating that YSFs inevitably solidify during wetting or spreading flows as the velocity gradually diminishes. The liquid–solid transition appears as a plateau at the rise curve, at a glance, but its re-rise occurs by a slip between the YSF and the inner wall surface. By assuming a depleted slip layer, the entire capillary rise curve could be predicted with a simple rheology model. The MATLAB code utilized for numerical calculations is readily accessible. Even if our demonstration is performed under ideal conditions without evaporation, the suggested model including DCA theory can provide crucial information about how YSFs flow inside channels at lower stresses, which is difficult to measure accurately, typically requiring a complicated force sensor or a micro-PIV device (Graziano *et al.* 2021). Our capillary imbibition model with experiments can be helpful to obtain parameters such as surface tension, slip length and dynamic wetting coefficients, required for wetting, spreading, simple pipe flow and any other slippery flow. Since predicting penetration rate and fluid uptake in porous media shares the same phenomena with capillary rise, our system can also provide clues for modelling YSF flow in porous media.

Acknowledgements. We are grateful to S. Han and the Korea Institute of Geoscience and Mineral Resources (KIGAM) for helpful discussions, and K.H. Kim and K. Lee for their comments on the manuscript.

Funding. This research was supported by the Basic Science Research Program through the National Research Foundation of Korea (NRF) (NRF-2021R1A6A3A13046176, NRF-2021R1A2C2009859, RS-2023-00276535) and the Korea Evaluation Institute of Industrial Technology (20014762).

Declaration of interests. The authors report no conflict of interest.

Code availability statement. The code proposed in this study is openly available in github at https://github.com/hanull15/capillary_ysf.

Author ORCID.
Hanul Kim https://orcid.org/0000-0003-3183-8917.

Appendix A. Experimental capillary rise measurement

Capillary rise experiments are performed using a glass capillary; $h(t)$ and $\theta(t)$ measurements and glass preparation follow our previous work, Kim *et al.* (2020). A borosilicate glass capillary was purchased from World Precision Ins. (Sarasota, FL). The aq. glycerol data shown in figure 1(*b*) are from a capillary with radius 0.42 mm. Other capillary radius conditions are given in table 1. The glass capillary was properly cleaned with a 1 M sodium hydroxylate (NaOH) solution at 75 °C, and rinsed with deionized water. Wet capillaries are dried in a vacuum oven for more than 1 hour. A CCD camera (EO-0413M 1/3" CMOS monochrome USB camera, 59-363 Edmund Optics) is used to record capillary rise video at a rate of 20 frames per second. Evaporation is prevented by enclosing the experimental set-up within an acrylic box equipped with a humidifier. During the capillary rise experiment, the YSF in the reservoir was not subjected to any additional shearing actions, like stirring or vortexing.

Purchased from Lubrizol and Sigma, respectively, Carbopol 940 NF polymer and xanthan are dissolved in water at concentrations between 0.08 wt. % and 1.3 wt. %.

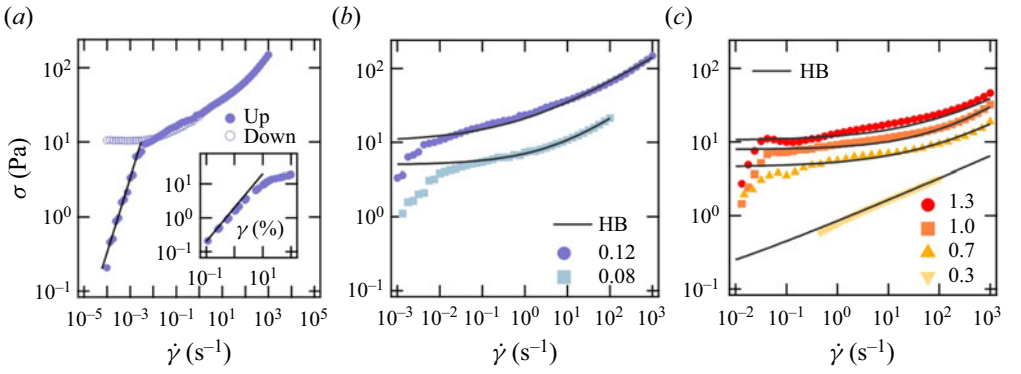

Figure 4. (*a*) Ramp-up and ramp-down cycles of shear-rate–stress measurement for Carbopol 0.12 wt. %. The inset is the corresponding stress–stress curve. Solid lines are for power 1. (*b*,*c*) The measured up-ramp cycles of shear rate versus stress flow curves for (*b*) Carbopol and (*c*) xanthan solutions. Concentrations in (*b*,*c*) are given in wt. %.

Polymeric solutions were mixed with a magnetic stirring bar under moderate rpm below 300 to prevent the scission of polymer strain, which is well known as critical for hindering viscoplastic properties (Dinkgreve *et al.* 2018). To fully hydrate the polymers, mixing is continued for more than 24 hours. Afterwards, the Carbopol solution pH is matched to 7 by adding 1 M NaOH drops to make the polymer strain swollen and have yield stress.

Appendix B. Rheology measurement

In figures 4(*a–c*), the stress–strain rate (σ–$\dot{\gamma}$) flow curve of the YSFs was measured using an MCR302 (Anton Paar Ltd) with a sandblasted PP25 plate. Before each test, all YSFs were pre-sheared with a stirring bar and rested for more than 1 hour to minimize the effect of shear history and obtain reproducibility. Shear stress is measured by controlling the shear rate, with the time interval between rates determined by reaching a steady state where stress stabilizes within a tolerance $\leq$1 nN m, typically averaging approximately 5 seconds. The initial deviation seen in ramp-up curves from the HB model corresponds to the elastic response phase. As figure 4(*a*) demonstrates, the minimal discrepancy between up-ramp and down-ramp above yield stress suggests that all samples behave as simple YSFs devoid of thixotropic properties. The minor fluctuation in xanthan solution shear rates ranging from 0.1 to 1 s^{-1} is likely due to local plastic deformations or multiple stress overshoots, reflecting the inherent microstructural inhomogeneity of the xanthan solution, even after adequate mixing. These fluctuations minimally impact capillary rise because the solid-to-liquid plastic deformation primarily occurs rapidly at the initiation of the measurement, and the shear rate diminishes over time, similar to a ramp-down approach. Although ramp-up data are presented to clearly depict the fit with the σ_{HB} model, the capillary rise process adheres to the HB curve fitted, as illustrated in figure 4(*a*). Measured parameters are detailed in table 1, and the rheological behaviour of aqueous glycerol is consistent with Kim *et al.* (2020), with the solvent viscosity set at 1 mPa s.

Appendix C.The DCA models

The DCA models describe the deviation of Laplace pressure from that at equilibrium ($h = h_E$) (Cox 1986). Thus the wetting friction is defined for the meniscus as

$$\Theta(t) = 2\pi R\Gamma(\cos\theta_E - \cos\theta(t)). \tag{C1}$$

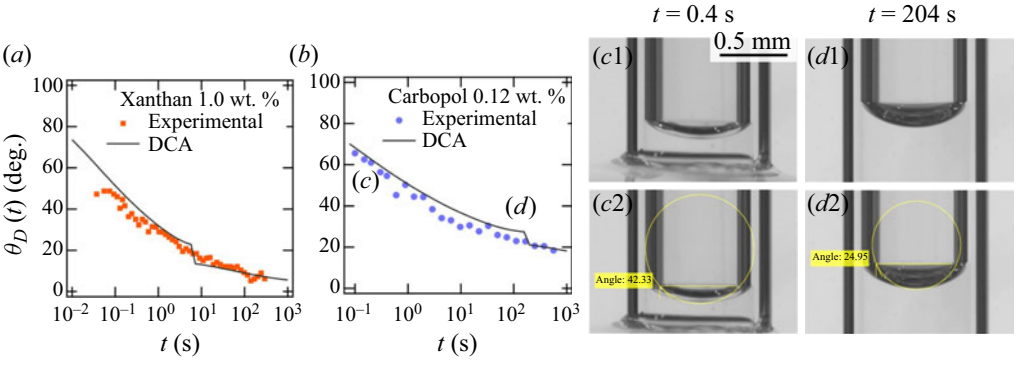

Figure 5. (*a*,*b*) The contact angle change during the capillary rise of (*a*) xanthan and (*b*) Carbopol. (*c*1,*d*1) The raw meniscus images of (*b*) before and after solidification. (*c*2,*d*2) The corresponding contact angle measurement results. The measurement method is validated in Kim *et al.* (2020).

In this paper, two different DCA models are combined for YSFs. Before the solidification, wall shear stress is assumed to be significantly larger than yield stress, working as shear thinning fluids:

$$\Theta_t(t) = -\chi_1 \frac{K}{R^{n-1}} \left(\frac{\dot{h}(t)}{\theta(t)} \right)^n, \tag{C2}$$

where χ_1 is a fitting parameter (Kim *et al.* 2020). After h_p, the wetting friction is assumed to be proportional to the slip stress as

$$\Theta_s(t) = -\chi_2 2\pi R\, d(t)\, \sigma_s(t) = -\frac{\chi_2 R\mu}{l_s} \frac{1-\sin\theta(t)}{\cos\theta(t)} \dot{h}(t), \tag{C3}$$

where parameter χ_2 is the proportional factor, σ_s is the slip shear stress at the meniscus, and d is the meniscus depth. When χ_1 and χ_2 are fitted from contact angle change (figures 5*a*,*b*) against capillary rise velocity, the DCA prediction agrees well with the experimental early rise velocity as shown in figures 3(*a*,*b*). Since the shear thinning model does not account for yield stress, the transition from simple shear DCA model to slip DCA model appears as a discontinuity at the solidification ($\sigma_w = \sigma_Y$).

Appendix D. The PIV measurement

We purchased 0.001 wt. % of 10 μm sized hollow glass sphere from Sigma and added to 0.12 % Carbopol. By conducting the same shear-rate–stress measurement given in Appendix B, we checked that the rheological properties of solution is not changed. The focus of image given in figure 2(*a*) is at the vertical midplane of the horizontal capillary by matching the focus plane to the capillary inner wall accurately. For the supply of fluid at the capillary end, the solution reservoir is placed at the same vertical height with the capillary. A polystyrene petri dish is used, with a hole on the wall to expose the solution's free surface to the capillary inlet.

Appendix E. The effects of shear banding and surface conditions

The deviation of the rise curve between xanthan solutions and our model prediction might be due to the localization of fluidity, commonly known as shear banding. Shear banding appears as bands of different shear rates even if the entire fluid is under the same

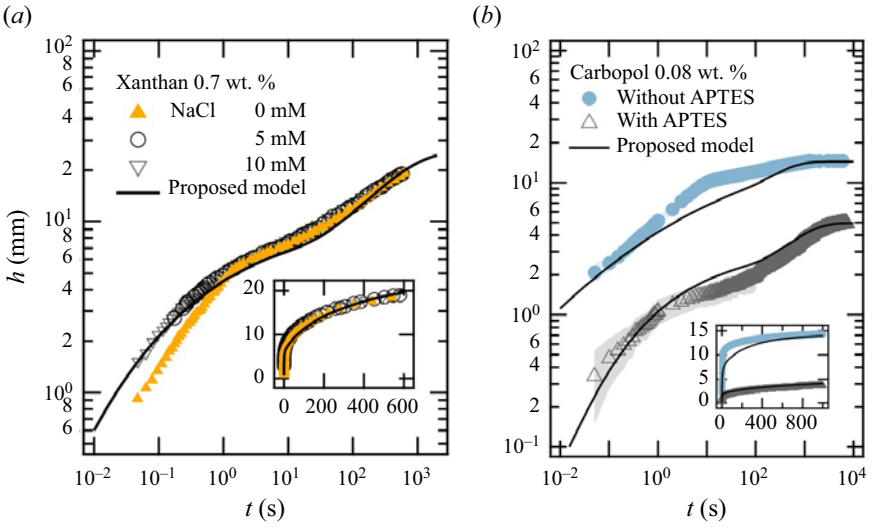

Figure 6. (*a*) Salt effects on the capillary imbibition of xanthan solutions. (*b*) Capillary rise on surfaces without (circle) and with (triangle) the APTES modification. The insets in (*a*,*b*) are the same curves in linear scale.

stress in simple Couette flow. This is known to be attributed to the inhomogeneity in the microstructure pronounced in polymeric gels.

To minimize the shear banding effect on xanthan solutions, the applied shear stress during capillary imbibition was delocalized by the addition of 5 and 10 mM NaCl Tang *et al.* (2018). As NaCl concentration increases, capillary imbibition aligns with the numerical model (figure 6*a*). This indicates that the shear banding effect could decelerate the initial stage of the capillary imbibition.

Also, we explored the capillary rise behaviour under a surface condition that is well known as no-slip. As emphasized in the main text, slip behaviour is crucial to understand the entire dynamics of capillary imbibition ($h(t)$). To further support the proposed theoretical model, we prepared silanized glass capillaries by adsorbing (3-Aminopropyl)triethoxysilane (APTES) to the surface of initial silanol. Dried capillaries were soaked in 5 v/v % APTES anhydrous acetone solution (Kiernan 2015). Because of high reactivity of APTES with water, silanization was conducted in a sealed vial without exposure to ambient humidity. The identical contact angles of the inner capillary surfaces indicated the homogeneity of the axial surface treatments.

A plateau region is observed at the APTES-modified surface as triangle markers in figure 6(*b*). By changing the surface to be less slippery, l_s decreased from 15 to 1 nm, and the plateau intensity (Δ, see main text for description) increased from 0.4 to 1.3. This shows that the surface well known as no-slip can also be described with extremely small l_s, thus the plateau appears regardless of the surface condition, including slippery and chemically or physically modified surfaces.

Although the previous study (Jalaal, Balmforth & Stoeber 2015) suggested that silanization could be an effective method to correct slip, it seems to be not valid for the faster flow condition. In order to suppress slip behaviour, the silanized ($-NH^{3+}$) surface should strongly attract negatively charged polymers; however, it will fail to create no-slip conditions in fast flows where hydrodynamic stress surpasses microscale electrostatic force. Salt dissolved in solutions could also weaken the electrostatic force. Moreover, slip correction using a rough surface frequently fails at pressure-driven pipe flow

(Liu & de Bruyn 2018) and at flow near a falling sphere (Holenberg *et al.* 2012). This evidence supports that the plateau may appear commonly in capillary imbibition with varying surface charges or roughnesses. Previous experimental studies on surface conditions named with no-slip might be the result of a shallow slip layer (l_s) close to the size of a single solvent molecule ($\leq$1 nm), following the dashed line in figure 3(c) of the main text.

For the APTES-modified surfaces, adjustments in model parameters were necessary: $\Gamma = 35\text{mN m}^{-1}$, $\theta_0 = 54^\circ$ and $\chi_1 = 3.5$. The reduction in hydrophilicity decreased Laplace pressure, consequently lowering the final rise height. Differences in surface tension values could be attributed to meniscus evaporation, acting as an additional frictional force (Zhang *et al.* 2017). The experiment did not use a humidifier for APTES-treated capillaries in order to prevent the formation of condensed water droplets on the glass surface, which would otherwise form an additional meniscus and negate Laplace pressure.

References

Balmforth, N.J. 2019 Viscoplastic asymptotics and other analytical methods. In *Lectures on Visco-Plastic Fluid Mechanics* (ed. G. Ovarlez & S. Hormozi). CISM International Centre for Mechanical Sciences, vol. 583, pp. 41–82. Springer.

Balmforth, N.J. 2022 Capillary rise of a viscoplastic fluid in a Hele-Shaw cell. *J. Non-Newtonian Fluid Mech.* **308**, 104878.

Balmforth, N.J., Frigaard, I.A. & Ovarlez, G. 2014 Yielding to stress: recent developments in viscoplastic fluid mechanics. *Annu. Rev. Fluid Mech.* **46**, 121–146.

Balmforth, N.J., Ghadge, S. & Myers, T. 2007 Surface tension driven fingering of a viscoplastic film. *J. Non-Newtonian Fluid Mech.* **142** (1–3), 143–149.

Barnes, H.A. & Walters, K. 1985 The yield stress myth? *Rheol. Acta* **24** (4), 323–326.

Benzi, R., Divoux, T., Barentin, C., Manneville, S., Sbragaglia, M. & Toschi, F. 2019 Unified theoretical and experimental view on transient shear banding. *Phys. Rev. Lett.* **123** (24), 248001.

Benzi, R., Divoux, T., Barentin, C., Manneville, S., Sbragaglia, M. & Toschi, F. 2021 Stress overshoots in simple yield stress fluids. *Phys. Rev. Lett.* **127** (14), 148003.

Bertola, V. 2009 Wicking with a yield stress fluid. *J. Phys.: Condens. Matter* **21** (3), 035107.

Bocquet, L., Colin, A. & Ajdari, A. 2009 Kinetic theory of plastic flow in soft glassy materials. *Phys. Rev. Lett.* **103** (3), 036001.

Bonn, D. & Denn, M.M. 2009 Yield stress fluids slowly yield to analysis. *Science* **324** (5933), 1401–1402.

Bonn, D., Denn, M.M., Berthier, L., Divoux, T. & Manneville, S. 2017 Yield stress materials in soft condensed matter. *Rev. Mod. Phys.* **89** (3), 035005.

Chaudhuri, P., Berthier, L. & Bocquet, L. 2012 Inhomogeneous shear flows in soft jammed materials with tunable attractive forces. *Phys. Rev.* E **85**, 021503.

Choi, J., Armstrong, M. & Rogers, S.A. 2021 The role of elasticity in thixotropy: transient elastic stress during stepwise reduction in shear rate. *Phys. Fluids* **33** (3), 033112.

Coussot, P. 2018 Slow flows of yield stress fluids: yielding liquids or flowing solids? *Rheol. Acta* **57** (1), 1–14.

Coussot, P., Nguyen, Q.D., Huynh, H.T. & Bonn, D. 2002 Avalanche behavior in yield stress fluids. *Phys. Rev. Lett.* **88** (17), 175501.

Coussot, P. & Rogers, S.A. 2021 Oldroyd's model and the foundation of modern rheology of yield stress fluids. *J. Non-Newtonian Fluid Mech.* **295**, 104604.

Cox, R.G. 1986 The dynamics of the spreading of liquids on a solid surface. Part 1. Viscous flow. *J. Fluid Mech.* **168**, 169–194.

Damianou, Y., Philippou, M., Kaoullas, G. & Georgiou, G.C. 2014 Cessation of viscoplastic Poiseuille flow with wall slip. *J. Non-Newtonian Fluid Mech.* **203**, 24–37.

Dey, B., Ortiz, W., Cleaves, H., McMaster, A., McConnell, J., Tjiptowidjojo, K., Grillet, A.M., Secor, R.B., Newell, P. & Rao, R.R. 2023 A level set approach for the computational study of a yield stress fluid filling a thin mold. *J. Non-Newtonian Fluid Mech.* **312**, 104987.

Dimakopoulos, Y., Pavlidis, M. & Tsamopoulos, J. 2013 Steady bubble rise in Herschel–Bulkley fluids and comparison of predictions via the augmented Lagrangian method with those via the

Papanastasiou model. *J. Non-Newtonian Fluid Mech.* **200**, 34–51. Special Issue: Advances in numerical methods for non-Newtonian flows.

DINKGREVE, M., FAZILATI, M., DENN, M.M. & BONN, D. 2018 Carbopol: from a simple to a thixotropic yield stress fluid. *J. Rheol.* **62** (3), 773–780.

DIVOUX, T., BARENTIN, C. & MANNEVILLE, S. 2011 Stress overshoot in a simple yield stress fluid: an extensive study combining rheology and velocimetry. *Soft Matt.* **7**, 9335–9349.

DONLEY, G.J., SINGH, P.K., SHETTY, A. & ROGERS, S.A. 2020 Elucidating the G'' overshoot in soft materials with a yield transition via a time-resolved experimental strain decomposition. *Proc. Natl Acad. Sci.* **117** (36), 21945–21952.

GARG, A., BERGEMANN, N., SMITH, B., HEIL, M. & JUEL, A. 2021 Fluidisation of yield stress fluids under vibration. *J. Non-Newtonian Fluid Mech.* **294**, 104595.

GÉRAUD, B., JØRGENSEN, L., PETIT, L., DELANOË-AYARI, H., JOP, P. & BARENTIN, C. 2014 Capillary rise of yield-stress fluids. *Europhys. Lett.* **107** (5), 58002.

GRAZIANO, R., PREZIOSI, V., UVA, D., TOMAIUOLO, G., MOHEBBI, B., CLAUSSEN, J. & GUIDO, S. 2021 The microstructure of Carbopol in water under static and flow conditions and its effect on the yield stress. *J. Colloid Interface Sci.* **582**, 1067–1074.

HOLENBERG, Y., LAVRENTEVA, O.M., SHAVIT, U. & NIR, A. 2012 Particle tracking velocimetry and particle image velocimetry study of the slow motion of rough and smooth solid spheres in a yield-stress fluid. *Phys. Rev.* E **86** (6), 066301.

HU, Y., BIAN, S., GROTBERG, J., FILOCHE, M., WHITE, J., TAKAYAMA, S. & GROTBERG, J.B. 2015 A microfluidic model to study fluid dynamics of mucus plug rupture in small lung airways. *Biomicrofluidics* **9** (4), 1–15.

HUILGOL, R.R., ALEXANDROU, A.N. & GEORGIOU, G.C. 2019 Start-up plane Poiseuille flow of a Bingham fluid. *J. Non-Newtonian Fluid Mech.* **265**, 133–139.

HUILGOL, R.R. & KEFAYATI, G.H.R. 2018 A particle distribution function approach to the equations of continuum mechanics in Cartesian, cylindrical and spherical coordinates: Newtonian and non-Newtonian fluids. *J. Non-Newtonian Fluid Mech.* **251**, 119–131.

HUILGOL, R.R., MENA, B. & PIAU, J.M. 2002 Finite stopping time problems and rheometry of Bingham fluids. *J. Non-Newtonian Fluid Mech.* **102** (1), 97–107.

JADHAV, K.D., ROSSI, P. & KARIMFAZLI, I. 2021 Motion onset in simple yield stress fluids. *J. Fluid Mech.* **912**, A10.

JALAAL, M., BALMFORTH, N.J. & STOEBER, B. 2015 Slip of spreading viscoplastic droplets. *Langmuir* **31** (44), 12071–12075.

JALAAL, M., SEYFERT, C., STOEBER, B. & BALMFORTH, N.J. 2018 Gel-controlled droplet spreading. *J. Fluid Mech.* **837**, 115–128.

JALAAL, M., STOEBER, B. & BALMFORTH, N.J. 2021 Spreading of viscoplastic droplets. *J. Fluid Mech.* **914**, A21.

JAWORSKI, Z., SPYCHAJ, T., STORY, A. & STORY, G. 2022 Carbomer microgels as model yield-stress fluids. *Rev. Chem. Engng* **38** (7), 881–919.

JØRGENSEN, L., LE MERRER, M., DELANOË-AYARI, H. & BARENTIN, C. 2015 Yield stress and elasticity influence on surface tension measurements. *Soft Matt.* **11** (25), 5111–5121.

KAMANI, K., DONLEY, G.J. & ROGERS, S.A. 2021 Unification of the rheological physics of yield stress fluids. *Phys. Rev. Lett.* **126** (21), 218002.

KIERNAN, J. 2015 *Histological and Histochemical Methods*. Scion Publishing.

KIM, H., LIM, J.-H., LEE, K. & CHOI, S.Q. 2020 Direct measurement of contact angle change in capillary rise. *Langmuir* **36** (48), 14597–14606.

VAN DER KOLK, J., TIEMAN, D. & JALAAL, M. 2023 Viscoplastic lines: printing a single filament of yield stress material on a surface. *J. Fluid Mech.* **958**, A34.

LANDRUM, B.J., RUSSEL, W.B. & ZIA, R.N. 2016 Delayed yield in colloidal gels: creep, flow, and re-entrant solid regimes. *J. Rheol.* **60** (4), 783–807.

LIU, Y. & DE BRUYN, J.R. 2018 Start-up flow of a yield-stress fluid in a vertical pipe. *J. Non-Newtonian Fluid Mech.* **257**, 50–58.

LUCAS, R. 1918 Ueber das Zeitgesetz des kapillaren Aufstiegs von Flüssigkeiten. *Kolloidn. Z.* **23** (1), 15–22.

MALKIN, A., KULICHIKHIN, V. & ILYIN, S. 2017 A modern look on yield stress fluids. *Rheol. Acta* **56** (3), 177–188.

MARTOUZET, G., JØRGENSEN, L., PELET, Y., BIANCE, A.-L. & BARENTIN, C. 2021 Dynamic arrest during the spreading of a yield stress fluid drop. *Phys. Rev. Fluids* **6** (4), 044006.

MATSON, G.P. & HOGG, A.J. 2007 Two-dimensional dam break flows of Herschel–Bulkley fluids: the approach to the arrested state. *J. Non-Newtonian Fluid Mech.* **142** (1), 79–94. Special Issue: Viscoplastic fluids: from theory to application.

MCCONNELL, J., ORTIZ, W., SUTHERLAND, J.C., NEWELL, P., GRILLET, A.M., MCMASTER, A.M., BHAKTA, R.B. & RAO, R.R. 2022 Computational modeling and experiments of an elastoviscoplastic fluid in a thin mold-filling geometry. *J. Non-Newtonian Fluid Mech.* **307**, 104851.

MØLLER, P.C.F., FALL, A. & BONN, D. 2009 Origin of apparent viscosity in yield stress fluids below yielding. *Europhys. Lett.* **87** (3), 38004.

OLDROYD, J.G. 1947 A rational formulation of the equations of plastic flow for a Bingham solid. *Math. Proc. Camb. Phil. Soc.* **43** (1), 100–105.

PÉREZ-GONZÁLEZ, J., LÓPEZ-DURÁN, J.J., MARÍN-SANTIBÁÑEZ, B.M. & RODRÍGUEZ-GONZÁLEZ, F. 2012 Rheo-PIV of a yield-stress fluid in a capillary with slip at the wall. *Rheol. Acta* **51** (11–12), 937–946.

PIAU, J.M. 2007 Carbopol gels: elastoviscoplastic and slippery glasses made of individual swollen sponges. *J. Non-Newtonian Fluid Mech.* **144** (1), 1–29.

RIDEAL, E.K. 1922 CVIII. On the flow of liquids under capillary pressure. *Lond. Edinb. Dublin Phil. Mag. J. Sci.* **44** (264), 1152–1159.

SIKORSKI, D., TABUTEAU, H. & DE BRUYN, J.R. 2009 Motion and shape of bubbles rising through a yield-stress fluid. *J. Non-Newtonian Fluid Mech.* **159** (1), 10–16.

SOCHI, T. & BLUNT, M.J. 2008 Pore-scale network modeling of Ellis and Herschel–Bulkley fluids. *J. Petrol. Sci. Engng* **60** (2), 105–124.

DE SOUZA MENDES, P.R. 2011 Thixotropic elasto-viscoplastic model for structured fluids. *Soft Matt.* **7** (6), 2471–2483.

TANG, H., KOCHETKOVA, T., KRIEGS, H., DHONT, J.K.G. & LETTINGA, M.P. 2018 Shear-banding in entangled xanthan solutions: tunable transition from sharp to broad shear-band interfaces. *Soft Matt.* **14** (5), 826–836.

TOKPAVI, D.L., MAGNIN, A. & JAY, P. 2008 Very slow flow of Bingham viscoplastic fluid around a circular cylinder. *J. Non-Newtonian Fluid Mech.* **154** (1), 65–76.

TSAMOPOULOS, J., DIMAKOPOULOS, Y., CHATZIDAI, N., KARAPETSAS, G. & PAVLIDIS, M. 2008 Steady bubble rise and deformation in Newtonian and viscoplastic fluids and conditions for bubble entrapment. *J. Fluid Mech.* **601**, 123–164.

WASHBURN, E.W. 1921 The dynamics of capillary flow. *Phys. Rev.* **17** (3), 273–283.

ZHANG, X., LORENCEAU, E., BASSET, P., BOUROUINA, T., ROUYER, F., GOYON, J. & COUSSOT, P. 2017 Wall slip of soft-jammed systems: a generic simple shear process. *Phys. Rev. Lett.* **119** (20), 208004.

ZHAO, B., *et al*. 2019 Comprehensive comparison of pore-scale models for multiphase flow in porous media. *Proc. Natl Acad. Sci.* **116** (28), 13799–13806.